Pergamon

Journal of Structural Geology, Vol. 17, No. 1, pp. 131 to 146, 1995
Copyright © 1994 Elsevier Science Ltd
Printed in Great Britain. All rights reserved
0191-8141/95 $9.50+0.00

0191-8141(94)E0032-T

Modelling of mantled porphyroclasts using non-Newtonian rock analogue materials

COEN E. TEN BRINK and CEES W. PASSCHIER*

Department of Structural Geology, Institute of Earth Sciences, Utrecht University, Budapestlaan 4, 3508 TA Utrecht, The Netherlands

(*Received* 16 *August* 1993; *accepted in revised form* 25 *February* 1994)

Abstract—The development of δ-type porphyroclasts was modelled experimentally in a circular transparent shear rig using crystalline rock analogue materials. Rectangular camphor objects embedded in a matrix of octachloropropane were deformed in simple shear flow. The camphor deformed into δ-objects with progressive deformation up to a shear strain of 100. The development of these δ-objects and of gradients of flow parameters in the matrix was followed from step to step during the deformation. The δ-objects in this experiment show stair-stepping of wings that did not occur in earlier experiments with Newtonian fluids. Analysis of the flow pattern indicates that this is due to an unusual flow perturbation geometry around the relatively rigid camphor objects which rotate more slowly than equivalent objects in Newtonian flow. The non-Newtonian rheology of the experimental materials may be responsible for this deviant behaviour. This implies that non-Newtonian fluids are better analogues than Newtonian fluids to study the development of structures in rocks with non-Newtonian rheology, since the geometry of the resulting structures can be different.

INTRODUCTION

Mylonite zones are important tectonic elements that accommodate much of the imposed deformation in the crust and mantle. The geometry of microstructures in mylonites is an important source of information on the development of mylonite zones and on the kinematics and dynamics of flow in them. However, microstructures can only yield reliable data if their development is properly understood. Mantled porphyroclasts, one of the more common mylonitic microstructures, consist of a core (the porphyroclast) and a deformed mantle that can have a complex, monoclinic geometry which is commonly used to determine sense of shear in mylonites. The mantle is thought to develop by recrystallization in the outer rim of a large parent grain, of which the porphyroclast is a relic. Relatively common are mantled feldspar porphyroclasts in quartz–feldspar mylonites (Passchier & Simpson 1986, Hooper & Hatcher 1988, Hanmer & Passchier 1991) and mantled pyroxene porphyroclasts in peridotites (Boudier *et al.* 1988). We investigated the development of mantled porphyroclasts by experimental modelling, in order to determine what data besides sense of shear can be derived from porphyroclast geometry.

Some of the most conspicuous mantled porphyroclast shapes are δ-objects, which have a characteristic spiral shape similar to a Greek letter δ (Fig. 3; Passchier & Simpson 1986). The development of δ-objects has been investigated by Passchier & Simpson (1986), Van Den Driessche & Brun (1987) and Passchier & Sokoutis (1993). Their work was based on natural δ-objects and on experimental deformation of deformable mantles around rigid objects in Newtonian fluids. The experimental set-up and materials used in these studies have a number of limitations: (1) only small finite strain values were reached in single experimental steps in experiments by Passchier & Simpson (1986) and Van Den Driessche & Brun (1987) whereas natural porphyroclasts commonly develop at high finite strain; (2) the shapes of the 'porphyroclasts' were circular (except for Van Den Driessche & Brun 1987) whereas natural objects usually have a more complex shape; (3) the 'porphyroclasts' were fixed in size—the central object could not add new material to the mantle by recrystallization; (4) matrix materials were Newtonian fluids (except for Passchier *et al.* 1993) whereas rocks commonly deform by power-law flow; (5) matrix materials were non-crystalline fluids whereas rocks are polycrystals that develop a crystallographic preferred orientation that may influence flow behaviour. We have tried to overcome these restrictions by means of a new, more evolved experiment.

In order to model the development of natural δ-objects in mylonites more closely, we carried out experiments on organic, crystalline rock-analogue materials with non-Newtonian rheology in which the matrix and the 'porphyroclasts' have different rheologies. The 'porphyroclasts' have an initial elongate, approximately rectangular shape and are subject to deformation and recrystallization. The experiments were carried out in a circular shear rig that has the advantage that very high strains can be obtained and that the deformation process can be observed in transmitted light down to the scale of individual grains.

*Present address: Institut für Geowissenschaften, Johannes Gutenberg Universität, 55099 Mainz, Germany.

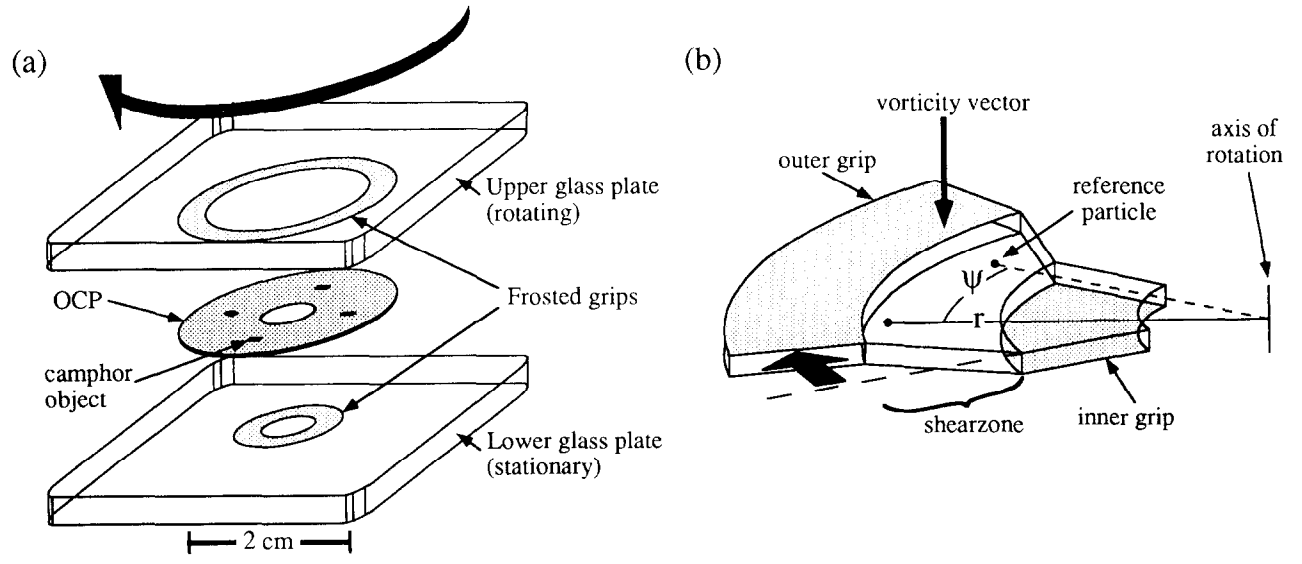

Fig. 1. (a) Simplified exploded view of the ring-shear apparatus. Sample material is contained between two glass plates. Clockwise rotation of the upper plate induces dextral sense of shear in the sample. (b) Detail of the deforming part of the sample material showing the location of shear zone development and explanation of the position of marker particles with respect to the rotational origin of the ring-shear apparatus and a certain reference particle.

MATERIALS AND METHODS

Apparatus

The ring-shear apparatus used in this experiment can model non-coaxial progressive deformation in a sample material. A sample is wedged between two glass plates (Fig. 1a) and is deformed in torsion by rotation of the upper glass plate around a central axis while the lower plate remains fixed. The sample can be observed through the glass plates during deformation under a petrographic microscope. An annular shear zone is created in the sample material by the presence of two frosted grips of different diameter, each etched on to one of the glass plates (Fig. 1a); since the sample material is only connected to the glass plates along the frosted grips, sample material in the annular shear zone is deformed in non-coaxial flow with the vorticity vector parallel to the rotation axis of the upper glass plate (Fig. 1b).

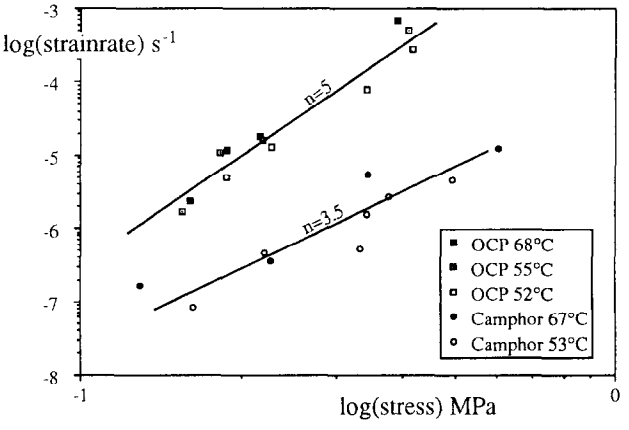

Fig. 2. Log (stress)–log (strain rate) plot for OCP and camphor with superposed lines for $n = 5$ and $n = 3.5$ in a power-law relationship: $\dot{\gamma} = C\sigma^n$. Unpublished data from A. Oostra.

Experimental materials

Two sample materials were used: octachloropropane (OCP) as a matrix material and camphor for porphyroclasts. OCP (C_3Cl_8) has a hexagonal crystal symmetry with a melting temperature of 160°C. Camphor ($C_{10}H_{16}O$) is either rhombohedral (<92°C) or cubic (>92°C) and its melting temperature is 179°C. The rheological behaviour of both materials between 52°C and 68°C was investigated experimentally by A. Oostra (Fig. 2, unpublished data). Both materials show power-law flow behaviour with stress exponents of approximately $n = 5$ (OCP) and $n = 3.5$ (camphor). Bons (1993) and Bons & Urai (1994) investigated the rheological properties at 28°C and found similar stress exponents of 4.5 ± 0.3 (OCP) and 3.3 ± 0.3 (camphor). Silicon carbide grit is distributed as a fine powder in the OCP and camphor and acts as marker particles for flow analysis.

Sample preparation

Sample preparation is similar to the technique described in Means (1983) and Jessell (1986). Approximately 5 g of laboratory grade OCP is chopped to a fine powder using a razor blade. It is mixed with 0.2% wt silicon carbide grit with an average particle size of 26 μm and pressed between teflon foil into a disk of approximately 0.4 mm thick and 25 mm in diameter using a hand operated press. The sample disk is optically checked for uniform distribution of the grit particles; if the distribution is far from uniform, the process of chopping and pressing is repeated. A camphor disk is prepared in the same way.

The surfaces of the two glass plates, except for the frosted grips, are coated with a thin film of silicon grease. This is done in order to reduce friction between the

deforming material and the glass plates; a sample will only deform homogeneously if it is not attached to the glass plates between the frosted grips. The OCP disk is pressed onto the glass plate with the larger frosted grip using a hand press. Excess material outside the larger grip and inside the smaller grip is removed. With a preparation needle four depressions are made in the part of the OCP that will be the future shear zone. Four slightly oblong pieces of approximately 0.4 × 0.4 × 0.5 mm are cut from the camphor disk and placed in the depressions. The voids around the camphor fragments are closed by addition of a small slice of OCP and gentle pressure on the sample.

The second glass slide is now emplaced on the sample material and the assembly is placed in the ring-shear apparatus which is then heated to 60°C (0.77 T_m of OCP) and left to anneal for 3 days. A dead weight of 3 kg, placed on the upper glass plate, is used to attain full contact between the sample material and the glass plates over the entire area of the frosted grips. During annealing, the thickness of the sample is reduced to approximately 0.3 mm. When complete contact is established between the sample and both glass plates, the top of the ring-shear apparatus is tightened so that a rubber ring applies a normal stress on the sample.

The resulting sample has no large voids and shows four approximately rectangular camphor objects in a homogeneous OCP matrix (Figs. 4 and 5a). For both OCP and camphor, average grain size after annealing is 0.1–0.15 mm, the grain shape is equidimensional, and grain boundaries are straight or slightly curved. There is no apparent grain-shape foliation, though sample preparation has probably introduced a weak crystallographic preferred orientation (Jessell 1986). The four oblong camphor objects are numbered C1–C4 and have initial aspect ratios (R_{xy}) of 2(C1), 1.4 (C2), 1.5 (C3) and 1.2 (C4). The initial angles between their long axes and the frosted grip circle are 6° (C1), 67° (C2), 53° (C3) and 95° (C4), respectively (Fig. 4).

EXPERIMENTAL CONDITIONS

A small motor was used to rotate the upper glass plate at a constant rate of 0.5 revolutions per hour, which imposed a bulk shear-strain rate ($\dot{\gamma}$) of about 2.6×10^{-3} (s^{-1}) over the annular shear zone between the frosted grips. This produced a relatively homogeneous, non-coaxial circular Couette flow in the OCP matrix in the shear zone. Flow lines are circular but parallel to the frosted grips and the flow pattern bears a resemblance to simple shear in that no stretching occurs parallel to the grips. We define a 'flow circle' as a circle parallel to the grips, similar to the 'flow plane' of simple shear.

The temperature was kept at 60 ± 0.5°C during the first 12 h of deformation. The motor was switched off for approximately 6 min at regular intervals to take photomicrographs of the sample. After the first 12 h of deformation, the imposed finite shear strain (γ) was about 113 (Fig. 6). γ is calculated as circular displacement of the outer frosted grip, divided by shear zone width (Passchier & Sokoutis 1993).

Several times during the experiment the sample seemed to break at the inner grip. In that case the motor and the temperature control were shut off and a dead weight of 3 kg was placed on the upper glass plate. After the contact was restored, the ring-shear apparatus was tightened and the sample heated up before restarting the deformation. These interruptions did not visibly affect the already developed microstructures in the zone around the camphor objects, though they did flatten the whole sample by a few μm.

EXPERIMENTAL OBSERVATIONS

Deformation of the OCP matrix

Soon after deformation started, a grain-shape preferred orientation (GSPO) developed in the OCP close to the inner grip while little deformation was visible in the rest of the sample. This zone of higher strain gradually widened during the experiment but the inner part of the shear zone retained the best grain-shape foliation. This means that finite strain was not homogeneously distributed over the sample but increased towards the inner grip. This effect results from the circular shape of the specimen chamber which induces a gradient of increasing flow stress and strain rate over the sample towards the inner grip. This gradient is an inherent property of any circular shear zone set-up. The foliation, defined by the GSPO, is at a small angle to the imposed flow circle in areas that are only little influenced by the camphor objects while it is deflected around the objects (Fig. 7).

Besides a GSPO, a crystallographic preferred orientation developed in the OCP matrix. The trace of the long axis of the indicatrix is preferentially perpendicular to the flow circle in the domain outside the zone of contact strain around the camphor objects. Near the top-left and bottom-right of the camphor objects, this trace is oriented approximately 30° counter-clockwise from the general orientation.

Deformation of the camphor objects

During the experiment the camphor objects deformed and rotated with respect to the flow circle. The initial rectangular objects (Figs. 4 and 5a) started to shed fine grained mantle material from their rims, probably by dynamic recrystallization (Fig. 5b). Up to $\gamma = 19$, this fine grained material stretched into the surrounding OCP matrix at the two opposite corners of the rectangular object that were in the extensional quadrant of the flow (Fig. 5c). With continuing deformation the other two corners rotated into a similar position and also started to shed material (Fig. 5e). The resulting 'wings' of fine grained material did not detach from the camphor core and with increasing deformation they stretched,

thinned and even 'wrapped around' the central object (Figs. 5f–l); they were smoothly curved and have a remarkably regular thickness. Embayments of OCP formed between the central object and the wings and caused the typical δ-shape. After initial development of the wings, the camphor objects did not shed any new fine grained material but continued to deform internally. The wings did not stretch along a single circular arc through the centre of the objects as would be expected, but show 'stair-stepping'; they 'step-up' over the object, similar to some natural mantled porphyroclasts (Lister & Snoke 1984, Passchier *et al.* 1993 and Passchier & Simpson 1986) (Fig. 3).

The set-up of our experiment allows not only direct observation of the change in geometry of a deforming object, but also allows quantification of deformation parameters based on the displacement of inserted silicon carbide marker particles (Means 1983, Jessell 1986). We used the displacement patterns to study: (1) the gradients of individual deformation parameters, and (2) the perturbation in the flow pattern around camphor objects.

DEFORMATION PARAMETER GRADIENTS

Tensor calculations

For any small area, confined by at least three marker particles for which the relative positions before and after a deformation increment are known, a local deformation tensor can be calculated (Ramsay 1967, Jessell 1986). Since the tensor describes a homogeneous deformation, we cannot resolve deformation inhomogeneities on a scale smaller than that between marker particles. In practice this means that we cannot calculate the difference in deformation behaviour for individual crystals in the sample. For the ring-shear apparatus we used a curvilinear reference frame (Fig. 1b) with the origin at the centre of rotation of the upper glass plate and a reference axis defined by the origin and one of the marker particles. The position of every marker particle at time (t) is thus defined by its distance to the origin (r) and its polar angle (ψ) to the reference particle (Fig. 1b).

In this experiment we use the following method to calculate the local deformation tensor (**F**) (Bons *et al.* 1993). A regularly spaced imaginary polar grid is superposed on the sample (Figs. 8a and 9a). The position of each grid node is defined with respect to four adjacent marker particles occupying at least three different quadrants. After a deformation step, these particles are displaced (Fig. 8b) and if one marker particle is used as a reference, the translation component of deformation can be deleted and the relative displacement of marker particles can be measured (Fig. 8c). A least squares best fit method is now used to determine the displacement of each grid node from the displacement of the four adjacent marker particles (Fig. 8c). Using this technique, a deformed polar grid can be constructed (Fig. 9b) and the deformation tensor for the deformation increment can be calculated for each individual grid node (Bons *et al.* 1993). A slight error in the determination of the position of a marker particle may introduce a significant error in the calculation of the finite strain tensor. This implies that the deformation increments should not be too small when this method is being used.

We studied deformation around camphor object C2. Enlarged photographs of C2 taken at 10 min intervals between 570 and 630 min of deformation (imposed γ of 89 and 98, respectively) were studied in detail. On each photograph over 1000 marker particles were traced, numbered and digitized. Inaccuracy in the orientation of enlarged photographs can cause a significant error in the rotational component of the deformation, therefore photographs of the entire specimen chamber (as Figs. 4 and 6) were used to determine the centre of rotation and the exact orientation of the enlarged photographs with respect to this origin. The results of an interval of 20 min running time [between 570 ($\gamma = 89$) and 590 ($\gamma = 92$) min] are presented as a deformed grid (Fig. 9b) and in plots showing the gradients of individual deformation parameters (Fig. 10). The increments from 590 to 610, and 610 to 630 min show similar results. The ring-shear apparatus was not tightened during these 20 min intervals.

Deformed grid

The undeformed and deformed grids in Fig. 9 show that flow is not homogeneously distributed over the annular shear zone in the sample, but partitioned: zones of high shear strain are located above and below the camphor object along the grips. Deformation of the camphor object is mainly a passive rotation: gradients of deformation intensity are rather small except in the region close to the object boundary. This is the domain where progressive deformation changes from a non-coaxial pattern towards rigid body rotation. The grid node spacing is too large to give an accurate estimate of the width of this transition.

Gradient plots

Since our experiment is virtually two-dimensional, the deformation tensor **F** can be fully described by only four independent coefficients, whose values depend on the chosen reference frame. However, **F** can also be expressed by four 'invariant' deformation parameters (see Appendix) such as finite strain R_f, a finite 'mean' vorticity number W_f (introduced in Passchier 1988 and there labelled W_n^m), finite dilatation A_f (the total area change) and the orientation of the long axis of the finite strain ellipse with respect to the flow circle (β_f). R_f is equal to (undeformed state) or larger than 1; A_f is 1 for absence of dilatation, and may be smaller (area decrease) or larger (area increase) than 1. W_f is a measure of the rotational component of the deformation normalized for strain (Appendix, Truesdell 1953, Passchier 1988). We use a positive sign for W_f to indicate a bulk clockwise rotation. W_f is 0 for a pure shear deformation history, 1

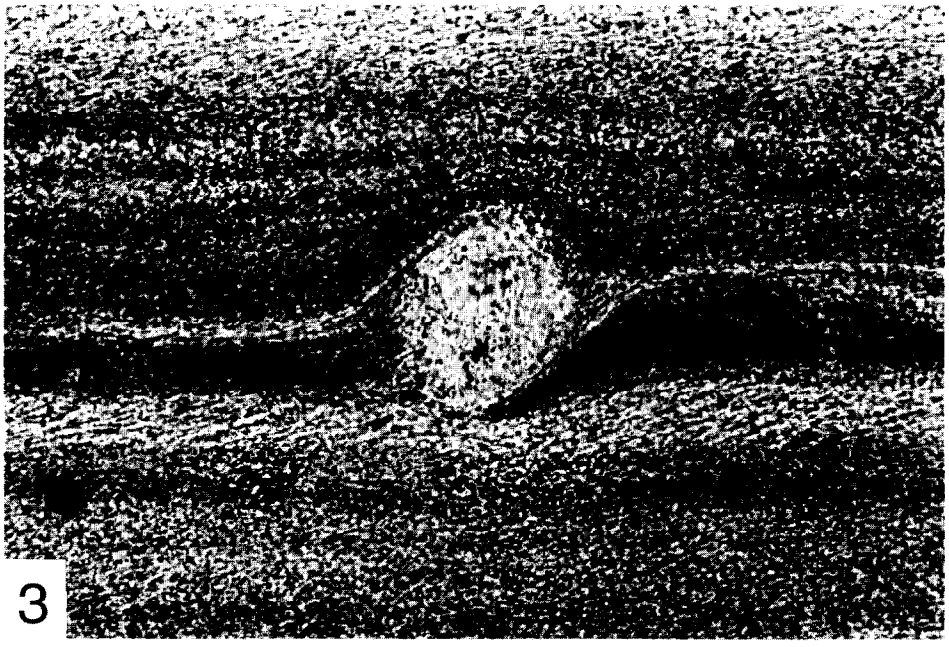

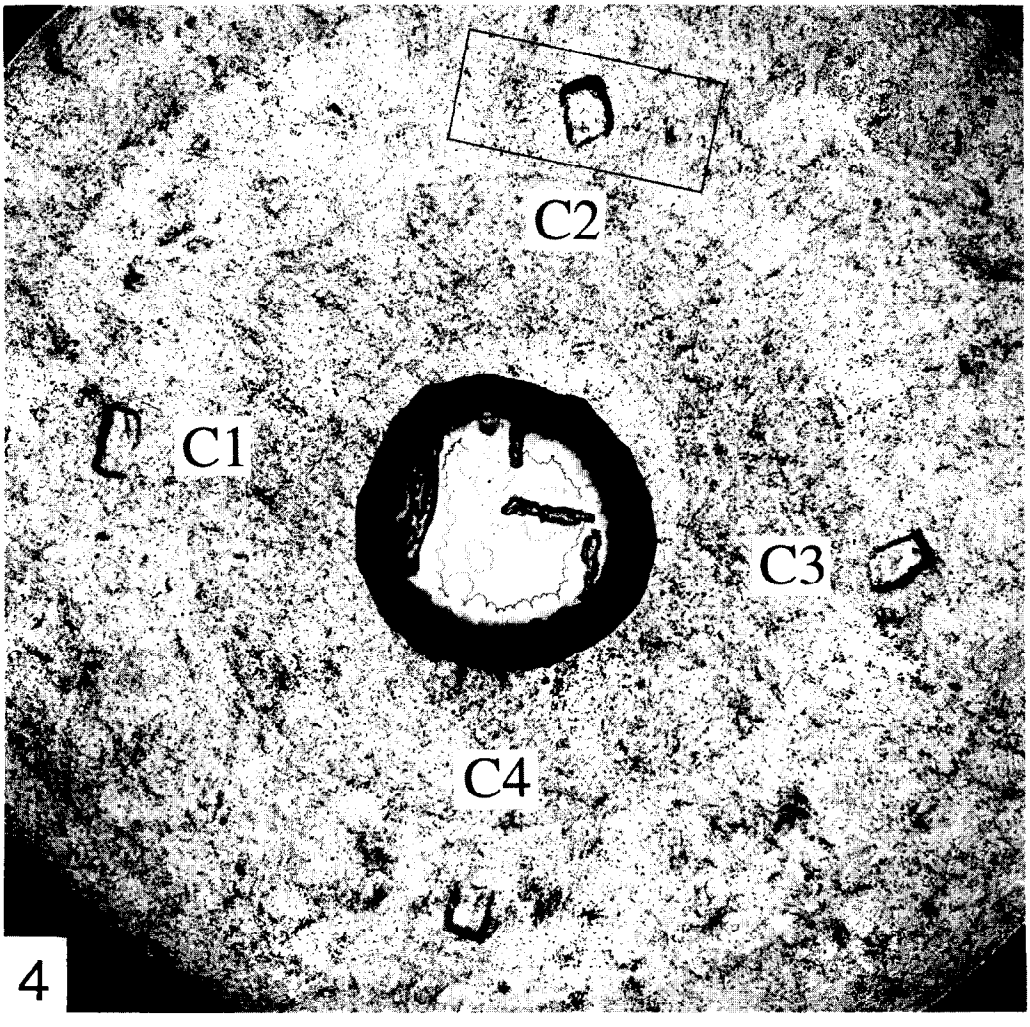

Fig. 3. Microphotograph of a plagioclase δ-porphyroclast in a matrix of quartz–plagioclase–biotite ultramylonite. The wings of recrystallized feldspar on both sides of the core show-stair-stepping. A weak mica preferred orientation is visible in the ultramylonite matrix. Barthélemy Massif, Pyrenees. Width of view is 3 mm, plane polarized light.

Fig. 4. Overview of the entire sample of OCP with camphor objects before deformation, seen from above. The width of view is 18 mm. Object numbers are indicated. 'Dust' in the sample are marker particles. The outline shows the area of Fig. 5(a). Plane polarized light.

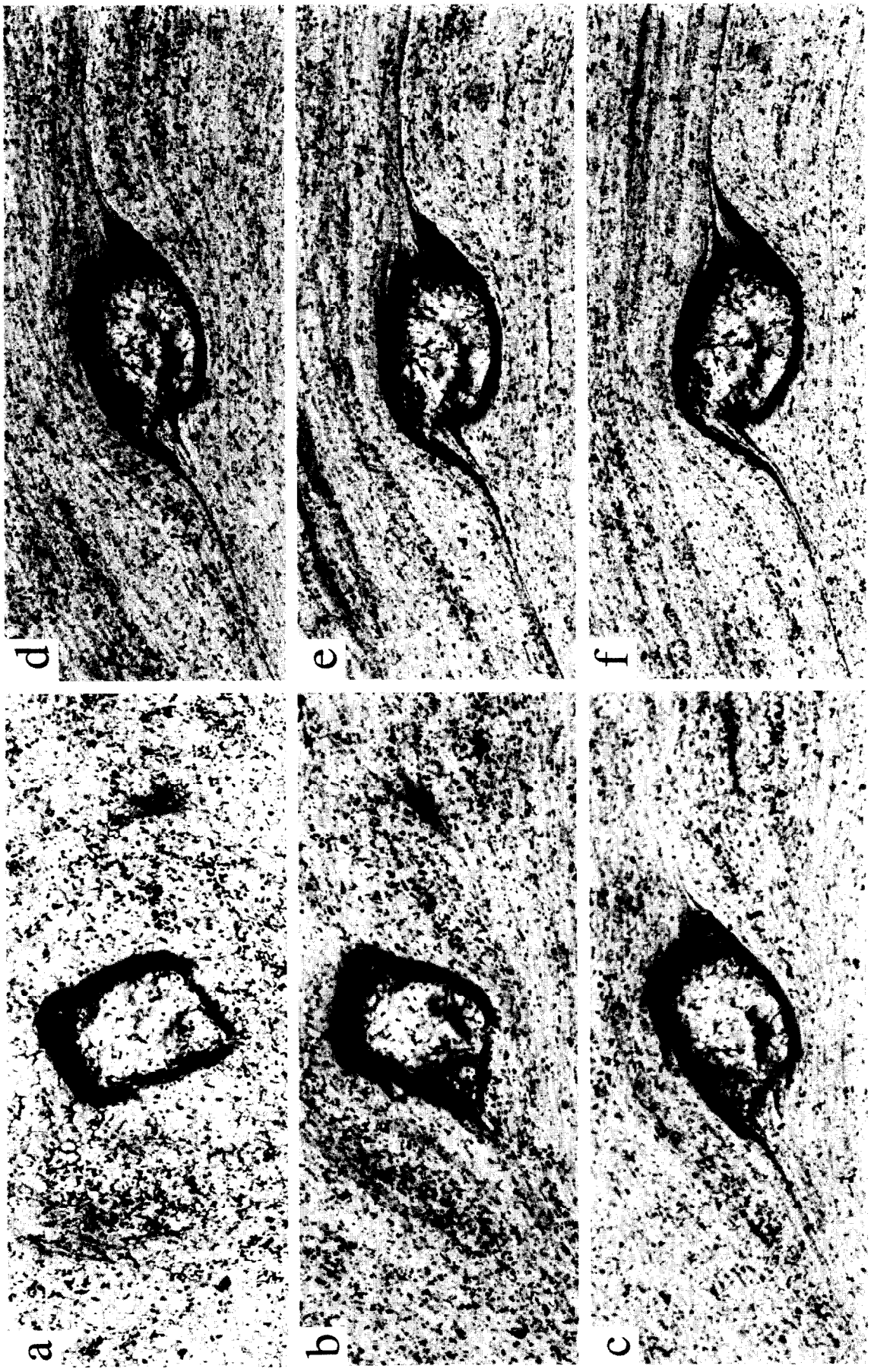
d
e
f
a
b
c

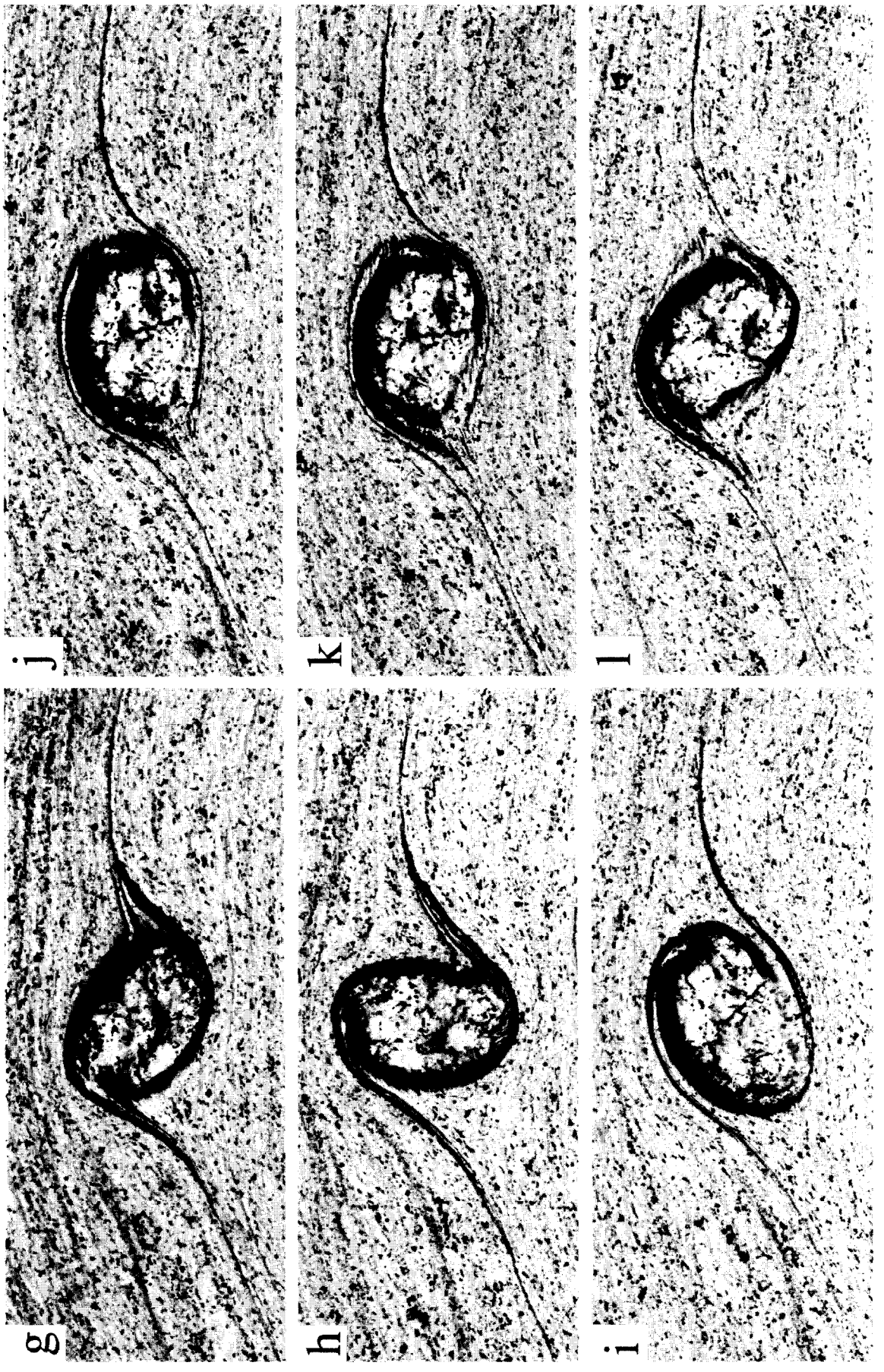

Fig. 5. Sequence of microphotographs of the camphor object C2 in plane polarized light, showing the gradual development of a complex δ-shape. The centre of rotation of the ring-shear apparatus is downward in all photographs. Running time and shear strain (γ) for these photographs was: (a) 0 min; $\gamma = 0$, (b) 60 min; $\gamma = 9$, (c) 120 min; γ=19, (d) 180 min; $\gamma = 28$, (e) 240 min; $\gamma = 37$, (f) 300 min; $\gamma = 47$, (g) 360 min; $\gamma = 56$, (h) 420 min; $\gamma = 66$, (i) 480 min; $\gamma = 75$, (j) 540 min; $\gamma = 84$, (k) 570 min; $\gamma = 89$, and (l) 630 min; $\gamma = 98$. The width of view is 4.5 mm.

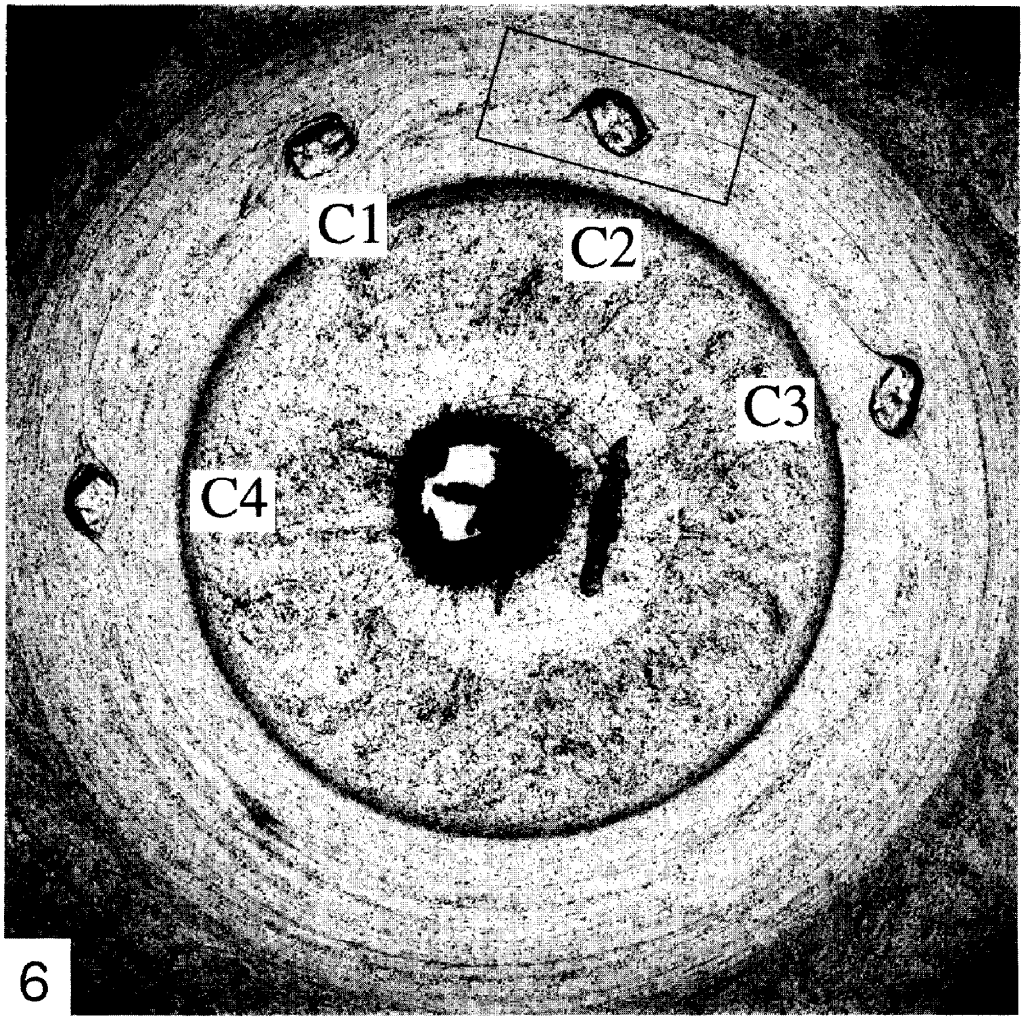

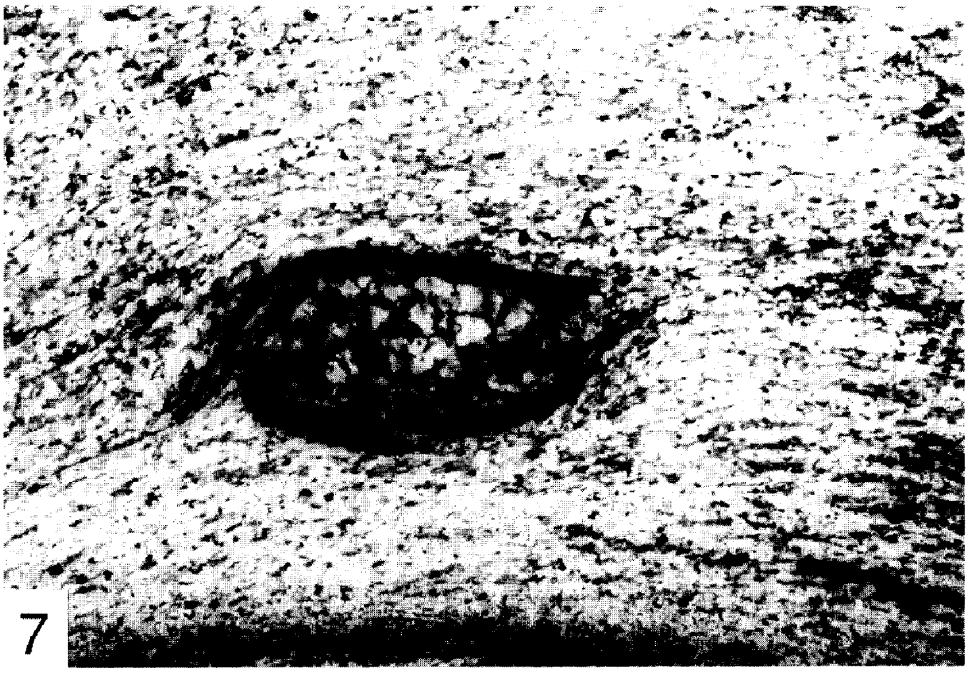

Fig. 6. Overview of the entire sample after 630 min of deformation ($\gamma = 98$). The width of view is 18 mm. Object numbers correspond to text and other figures. The area of Fig. 5(l) is outlined. Marker particles in the shear zone have been aligned while those outside are still undisturbed. Camphor objects have drifted together due to a difference in distance to the centre of rotation of the ring-shear apparatus. Plane polarized light.

Fig. 7. Microphotograph of C3 at 180 min running time ($\gamma = 28$) showing the grain shape preferred orientation of the matrix material around the object. Crossed nicols at 45° to the sides of the photograph; the width of view is 4.5 mm. Note that this is not the same object as the one shown in Fig. 5.

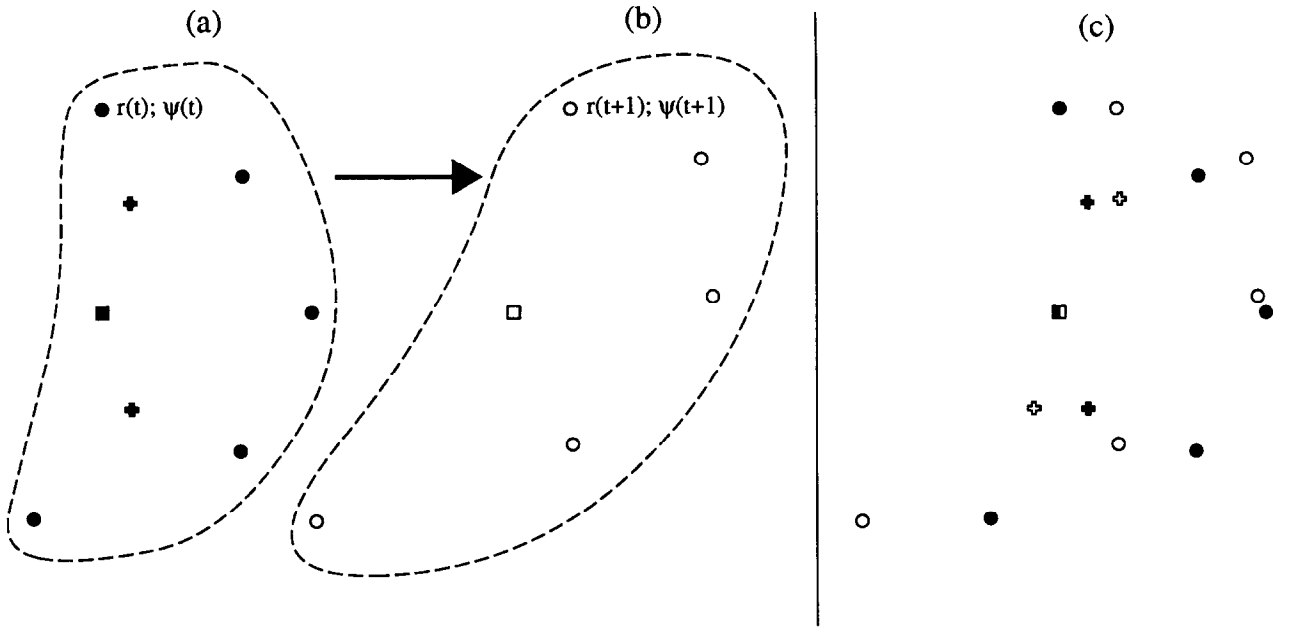

Fig. 8. Information used to calculate the deformation tensors and the position of grid nodes for a deformation increment. (a) Particles and grid nodes before the deformation increment. (b) Particles after the deformation increment. (c) Superposition of the two states with the reference particle as local origin. Circles—marker particles; square—reference particle; crosses—grid nodes; open symbols before deformation increment; closed symbols: after deformation increment. r and ψ are polar coordinates of grid points as shown in Fig. 1(b).

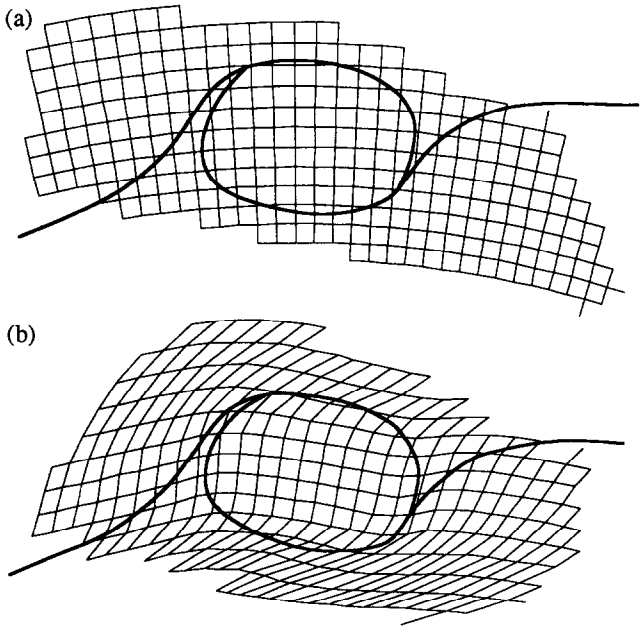

Fig. 9. Example of (a) an undeformed polar grid superposed on the sample material and object C2 after 570 min of deformation. (b) The deformed polar grid of (a) after an extra increment of 20 min of deformation. The outline of object C2 is indicated by a solid line. An increment of 20 min imposes a shear strain of approximately 3 over the entire shear zone: due to shear localization at the inner grip, the shear strain over the shear zone segment outlined by the grid is about 1.

for a dextral simple shear deformation history and goes to infinity for a rigid body rotation. We have chosen to use these four parameters because, although they are not independent, they completely describe the finite deformation, do not change with reference frame orientation and are easier to understand as physical entities than four coefficients that depend on reference frame.

Figure 10 shows the gradients of the four deformation parameters of **F** and shows the amount of detail about heterogeneous deformation that can be made visible with our method. The plots represent an interval of 20 min; though the imposed strain is 3, the strain is about 1 over the grid which only displays part of the shear-zone width.

The contour plot of R_f (Fig. 10a) shows values around 1 within the camphor object, and values exceeding 2.5 in bands parallel to the grips above and below the object; finite strain increases towards the inner grip due to the circular shape of the specimen chamber (Passchier & Sokoutis 1993).

The contour plot of W_f (Fig. 10b) shows high values within the object that indicate approximately rigid body rotation conditions. Values around 1, which represent simple shear, are located below the object, and away from it to the left and right. Interesting are domains of *negative* W_f on each side and close to the object that represent anticlockwise rotation. These domains of 'inverse' vorticity were theoretically predicted by Masuda & Ando (1988) and arise from the fact that the drag-effect of the rotating object on the matrix in the strain shadow is negative and locally exceeds the 'positive' vortical effect of bulk simple shear.

The contour plot of A_f (Fig. 10c) shows a mean value of 1 with some small local deviations. The specimen chamber is closed and volume should be conserved during deformation. Finite dilatation is therefore a function of changes in thickness of the specimen, or development of voids in the sample; an overall thickening or thinning of the sample material would result in a relatively constant deviation of a dilatation value of 1. The material is (nearly) incompressible at the stresses

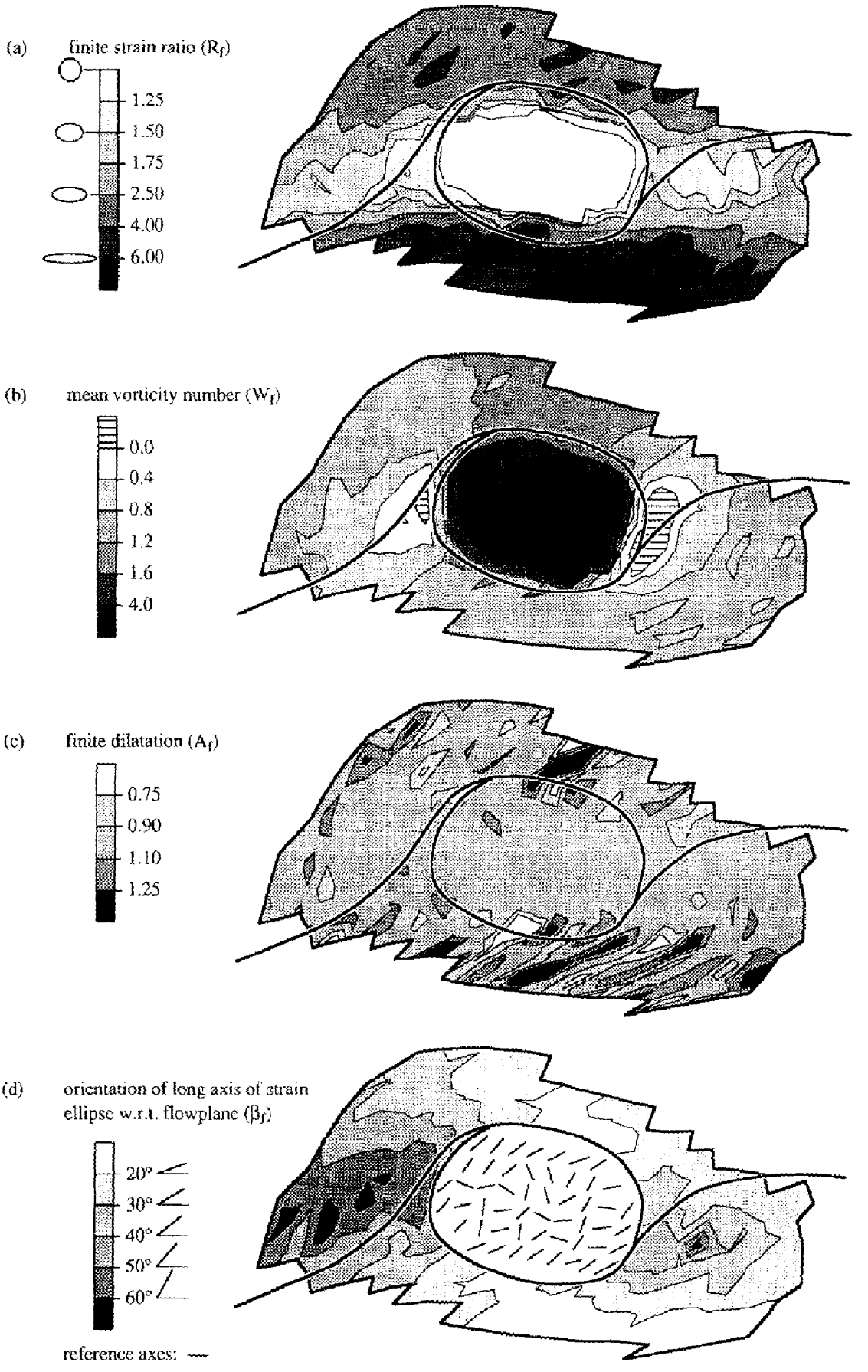

Fig. 10. Contour plots of (a) R_f, (b) W_f, (c) A_f, and (d) β_f for the deformation increment between 570 and 590 min running time around object C2, shown as a deformed grid in Fig. 9. The area within the elast in (d) shows the actual long axes instead of contours due to the large variation in orientation. The reference axis in (d) has unit length.

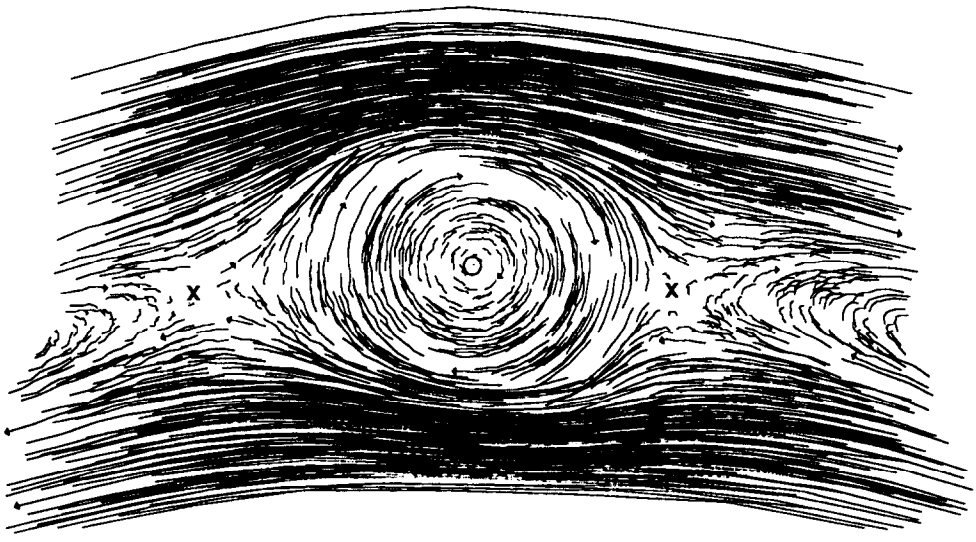

Fig. 11. Streamline pattern of the marker particles around C2 for six successive intervals of 10 min of deformation (between 570 and 630 min running time); sense of shear is dextral. Crosses are hyperbolic stagnation points; circle is parabolic stagnation point.

applied in this experiment and few voids develop within the shear zone. The local dilatation values can therefore be used as an indication of the errors made by tracing the exact positions of the marker particles.

The plot of β_f (Fig. 10d) shows the orientation distribution of the long axes of the strain ellipse with respect to the flow circle at the end of the deformation increment. It agrees well with the patterns of grain shape orientation visible in Fig. 7. In the camphor object, the large variation in β_f values can be attributed to the fact that strain is small here. This variation is probably the combined effect of small errors in locating the marker particles and small inhomogeneities in the deformation.

FLOW PERTURBATION

The presence of a rigid object causes perturbation of homogeneous flow. In a non-coaxial flow a rigid object will rotate if no shear localization occurs (Jeffery 1922). Rotation of the rigid object is associated with the generation of circular or ellipsoidal flow lines in the adjacent matrix; such flow lines can be approximately closed, i.e. a particle on a flow line will return approximately to its initial position. Somewhere in such a flow pattern there must be a transition between the open flow lines of far-field flow and closed flow lines. Such a transition is a sharp boundary known as a 'separatrix' (Ottino 1989).

Tracing of the relative displacement of marker particles can give a good indication of the pattern of flow around the camphor objects. Figure 11 shows the streamline pattern (the paths of individual particles as seen by an observer fixed to the reference frame for a reference particle at the centre of the object) around object C2 for six successive increments of 10 min of deformation. The pattern shows deflection of the open streamlines of simple shear away from the central object and ellipsoidal closed streamlines close to the object, as predicted by Ottino (1989). A separatrix can be envisaged between both domains and an additional domain of curved streamlines exists on either side of the object. This 'bow-tie shaped' flow perturbation pattern has three separatrices which end on two 'immobile' points (particles without relative displacement) on both sides of the central object. Such 'immobile' points are common where separatrices meet, and are known as 'hyperbolic stagnation points' (Ottino 1989, Passchier 1994). Material points on the separatrices move towards and away from such hyperbolic stagnation points.

MODEL FOR DEVELOPMENT OF COMPLEX δ-OBJECTS

Passchier *et al.* (1993) argued that a 'bow-tie' flow pattern will result in stair-stepping δ-objects when the ductile mantle of a rigid circular object is situated partly outside the separatrix. Such a flow pattern, however, cannot result in a more complex shape of the porphyroclast, like the double wings on either side of the object which started to develop after an imposed shear strain of 28 (Fig. 5d). Passchier & Simpson (1986) modelled the development of mantled porphyroclasts and succeeded in reproducing the double-winged examples sometimes found in nature by an instantaneous decrease in diameter of the rigid object. The 'mantle' of their clasts consisted of matrix material and the wings evolved from a passive marker line drawn on the matrix.

Our experiment shows both a bow-tie flow pattern and a core decreasing in diameter. The camphor objects are deformable and develop from a rectangular shape into an elliptical core with curved wings. The flow pattern can therefore be expected to have changed with time; this change in flow geometry has been found in the interval between 570 and 630 min running time (the experiment did not yield enough data to study the flow in detail over the whole time span). This makes it possible that parts of a clast that were at first 'trapped' within the

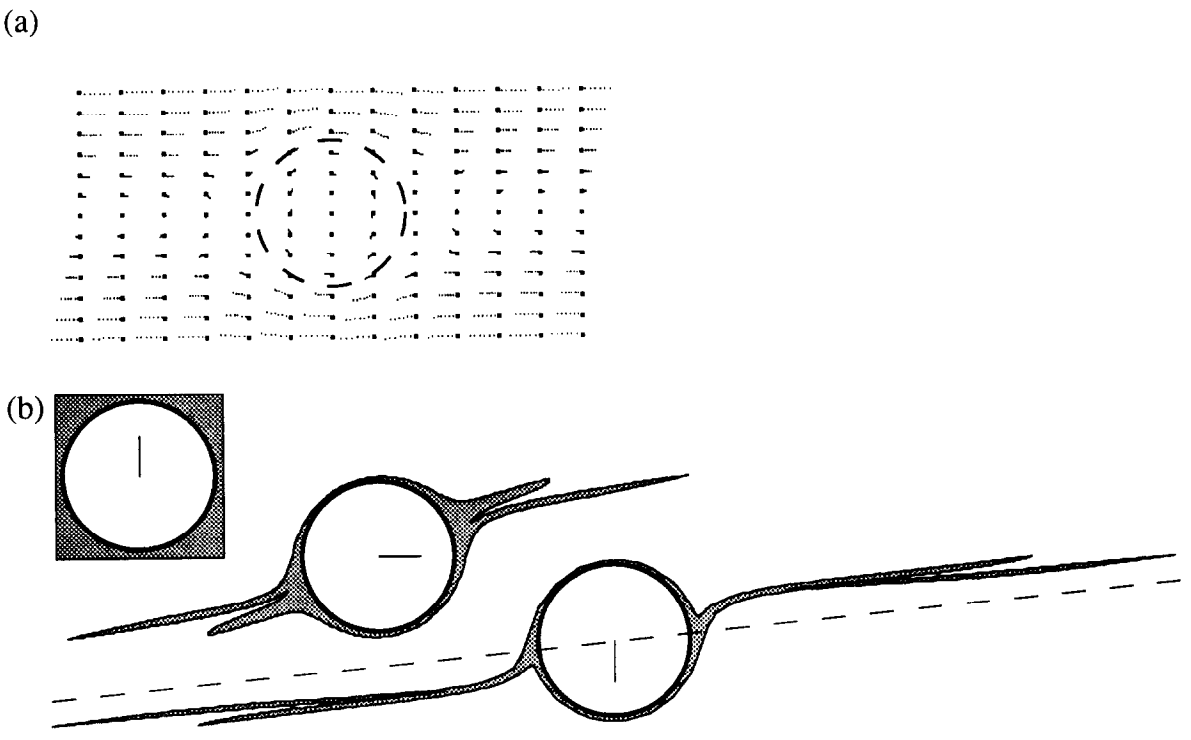

Fig. 12. (a) Particle displacements for six strain increments in a computer-generated, time-independent, deformation with a bow-tie pattern: heavy dots denote original positions; dashed circle indicates position of rigid object. (b) Evolution of a rigid circular object with a passive square mantle into a double winged stair-stepping δ-clast when subjected to deformation according to flow in (a). The dashed line through the centre of the rigid body is shown to clearly illustrate the stair-stepping geometry of the wings.

domain of elliptical flow lines became part of the domain of open flow lines, thus forming the base of a new generation of wings (Passchier 1994).

In our experiment, the observed small change in the flow pattern alone cannot account for the secondary set of wings as the geometry of the separatrix adapts to the orientation of the elliptical core. During a 90° rotation not enough 'mantle material' had been located far enough from the core to eventually 'escape' the central domain of the separatrix.

Due to stress concentration, the corners of a rectangular clast are more susceptible to degradation than the core. In our experiment this would make the camphor objects act as an elliptical core with a rectangular, more or less passive mantle. Computer modelling of a square passive marker around a circular rigid object shows that stair-stepping δ-objects with double wings can develop in a time independent 'bow-tie' flow pattern (ten Brink *et al.* 1993; Fig. 12).

OBJECT ROTATION RATE

Rigid ellipsoidal objects in a Newtonian fluid subject to simple shear flow rotate at a variable rate (Jeffery 1922). When an object lies with its long axis parallel to the flow plane the rotation rate has a minimum value, and when the long axis is perpendicular to the flow plane it has a maximum value. The variation in rotation rate is also proportional to the aspect ratio (R_{xy}) of the object (Jeffery 1922, Simpson & De Paor 1993). A circular object has a constant rotation rate, while objects with increasing R_{xy} values show an increasingly pulsating character.

We have monitored the rotational behaviour and change in shape of the oblong camphor objects in our experiment. Only the shape of the core was measured; the developing wings were not taken into account. Figure 13 shows the orientation of the object long axis with time. Figure 14 shows the theoretically expected and experimentally determined rotation rates against object orientation. The objects show a pulsating rotation rate and the orientation at which the experimental minimum and maximum values occur, parallel and perpendicular to the flow plane, respectively, fit well with the theoretically expected values for elliptical objects in a Newtonian fluid. However, the rotation rate of the objects in our experiment is relatively small compared to theoretically expected values for objects with the same aspect ratio (Fig. 14). Figure 15 shows the comparison of our results with other values; again, our experiment shows consistently low rotation rates. Recent experiments by Passchier and Sokoutis also give a first indication of lower rotation rates in non-Newtonian material (Passchier & Sokoutis personal communication).

Besides the rotation rate, the aspect ratio of the camphor objects changes with progressive orientation; it varies with time as the object is periodically shortened and extended in response to its orientation in the incremental flow field. Such behaviour can be expected in non-coaxial flow (Simpson & De Paor 1993). Another deviation from the theoretical model is that the

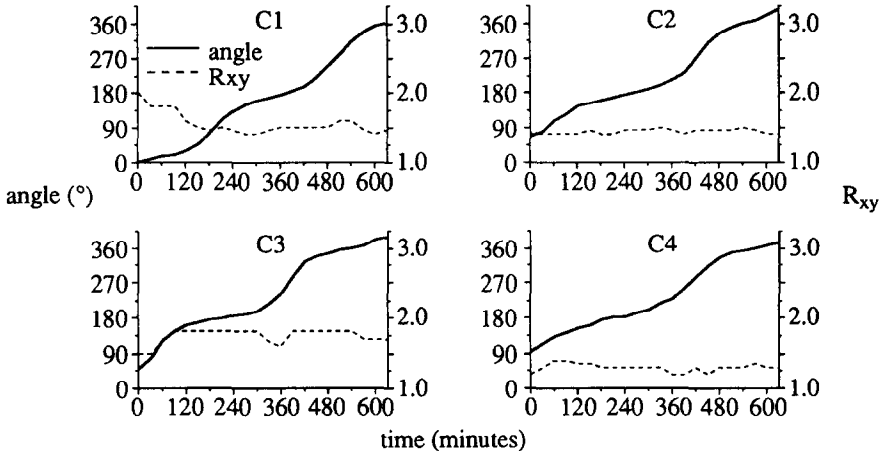

Fig. 13. Graphs showing the orientation of the long axis (solid line) and change in shape (dashed line) of the objects plotted against deformation time. See Fig. 14 for explanation of orientation.

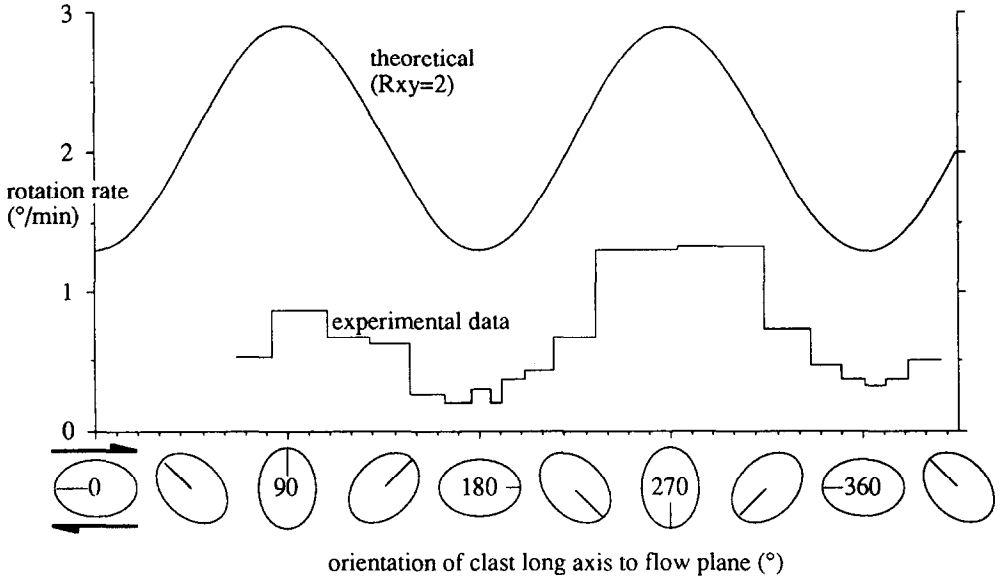

Fig. 14. Graph showing rotation rate vs angle the object long axis makes with the flow circle. The lower curve shows the mean experimental values. The upper curve shows the rotation rate of an elliptical object with an aspect ratio of 2 subjected to Newtonian simple shear at $\dot{\gamma} = 2.6 \times 10^{-3}\,(s^{-1})$.

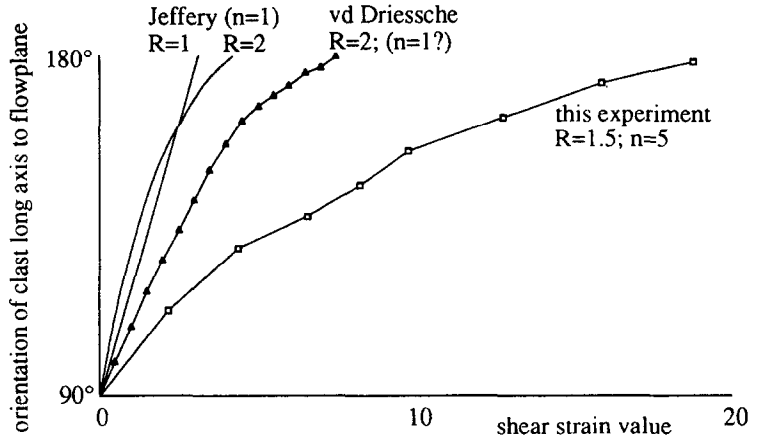

Fig. 15. Graph of orientation vs shear strain showing the difference in rotational behaviour of objects in simple shear flow. Shown are theoretical data derived from Jeffery (1922), data from an experiment by Van Den Driessche & Brun (1987) and data from object C2 in this experiment. R = length/width of the object; n = stress exponent of power law flow.

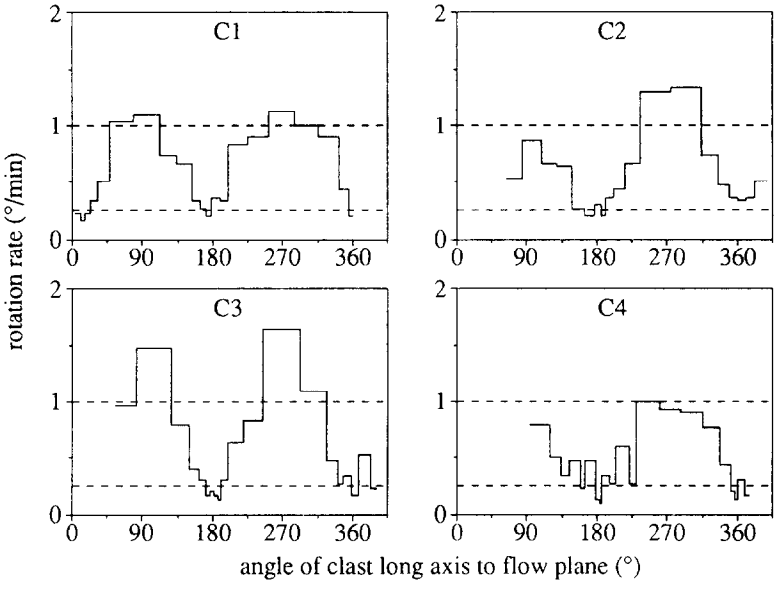

Fig. 16. Graphs showing the mean rotation rate vs orientation for all four objects.

minimum rotation rate does not seem to depend on the R_{xy} value of the objects (Fig. 16). This may be due to the existence of the wings which make the objects respond as if they had higher R_{xy} values when they are positioned with the long axis parallel to the flow plane.

DISCUSSION

The results of our experiment partly confirm those of earlier work with Newtonian fluids, but also shows a number of differences that are partly due to the experimental set-up that we have chosen. In our case, wings of δ-objects develop from material created in the rim of deformable objects that were homogeneous at the onset of the deformation. This may be comparable to the development of natural mantled porphyroclasts that form by development of a core and mantle structure, and subsequent deformation of the recrystallized mantle. It is difficult to explain, however, why recrystallization in our experiment was restricted to the initial stages of deformation. It may be due to the stress gradient set-up by the rectangular object; this stress gradient would cause stress concentration at the corners of the rectangles. After the object obtained a rounded shape, recrystallization may have stopped.

The high shear strain values reached in our experiments serve to illustrate that once a δ-object is established, and if the central object does not recrystallize further, the δ-shape is stable up to high strain. The wings wrap in an elliptical way around the central object, and eventually thin to such an extent that they become almost invisible (Figs. 5l and 6). This confirms the model proposed by Passchier & Simpson (1986).

During the experiment, a strong crystallographic preferred orientation developed in the crystalline OCP matrix. However, no change in the symmetry of the flow patterns or in the distribution of incremental strain values and orientations was observed to coincide with this development. It seems that, at least in our experiment, the development of a crystallographic preferred orientation in the matrix has little influence on the history of development of δ-objects.

The ellipsoidal shapes of the porphyroclasts did not have a significant effect on the development of wings, but the porphyroclasts did show the expected pulsating rotation rate of elliptical objects.

Our experimental results differ from those of previous workers in two important aspects: 'bow-tie' shaped flow perturbations developed around the objects, rather than the 'eye-shaped' perturbations expected theoretically and observed in earlier experiments; and camphor objects rotated significantly more slowly than theoretical expectations and other earlier experiments.

One of the main differences between the rheology of our sample materials and those of other workers is that ours are strongly non-Newtonian, and follow power-law behaviour (Fig. 1; Bons & Urai 1994). It is therefore possible that the non-Newtonian behaviour of our materials is responsible for the deviant behaviour. Experimental work by C. Passchier and D. Sokoutis (Passchier *et al.* 1993) on Newtonian and non-Newtonian non-crystalline fluids suggests that stair-stepping mantled objects only form in non-Newtonian fluids. Newtonian fluids give wings that are in line and lack stair-stepping. Observations on the rotation rate of a spherical rigid central object in the mantles of objects studied by Passchier *et al.* (1993), show that these objects also rotate more slowly than would be theoretically expected, though not as slowly as the values obtained in the experiment of this paper. The set-up of our experiments, however, makes it possible that the camphor objects were subject to drag against the glass slides and the effect may therefore partly be caused by drag and partly by the non-Newtonian nature of the OCP matrix.

CONSEQUENCES FOR THE INTERPRETATION OF NATURAL δ-OBJECTS

Our experiment shows that natural δ-objects can be successfully modelled if high strain values are accumulated by non-coaxial flow. This experiment indicates that δ-objects with shapes like Figs. 5(g) & (h), which are relatively common, must have experienced a considerable amount of shear strain to develop. However, quantification of shear strain from natural δ-objects is generally difficult since deformational conditions (rheologies of matrix and object, strain rate, homologous temperature, etc.) are usually unknown. δ-objects with spiral wings as shown in Figs. 5(i)–(l) are comparatively rare, possibly because such high strain values are not often reached in nature.

CONCLUSIONS

The flow perturbation around camphor objects in a non-Newtonian matrix of OCP subjected to overall simple shear has a bow-tie shape which is different from that predicted theoretically and observed experimentally for Newtonian fluids. As a consequence of the bow-tie shaped perturbation, the δ-objects in our experiment develop a stair-stepping geometry. The wings of the δ-objects spiral around the central object and gradually become thin and vague with progressive deformation, since no material can be added to the wings while they continue to stretch. Deformation is strongly variable around a developing δ-object; it ranges from approximately simple shear in the far-field to nearly rigid body rotation within the porphyroclast. Rotation rates of the porphyroclasts are relatively low when compared to theoretical values for elliptical objects in Newtonian fluids.

This experiment shows that non-Newtonian, crystalline analogues give more and better information than Newtonian fluids, as the geometry of the resulting structures can be different.

Acknowledgements—We thank Paul Bons and Mark Jessell for writing the application 'Marker Analysis' and refining it to our needs. C. E. ten Brink thanks Paul Bons for the endless discussions on deflection and his effort to create the program that generated Fig. 12. J. Van Den Driessche and an anonymous reviewer are thanked for their comments on the original manuscript. T. H. Bell encouraged us to do this experiment by his critical remarks on rotation.

REFERENCES

Bons, P. D. 1993. Experimental deformation of polyphase rock analogues. Publ. Ph.D. thesis, Utrecht University, the Netherlands. *Geologica Ultraiectina* **110**.

Bons, P. D., Jessell, M. W. & Passchier, C. W. 1993. The analysis of progressive deformation in rock analogues. *J. Struct. Geol.* **15**, 403–413.

Bons, P. D. & Urai, J. L. 1994. Experimental deformation of 2-phase rock analogues. *J. Mat. Sci. Eng.* **A175**, 221–229.

Boudier, F., Ceuleneer, G. & Nicolas, A. 1988. Shear zones, thrusts and related magmatism in the Oman ophiolite: initiation of thrusting on an oceanic ridge. *Tectonophysics* **151**, 275–296.

Hanmer, S. & Passchier, C. W. 1991. Shear-sense indicators: a review. *Geol. Surv. Can. paper* **90-17**, 1–72.

Hooper, R. J. & Hatcher, R. D. 1988. Mylonites from the Towaliga fault zone, central Georgia: products of heterogeneous non-coaxial deformation. *Tectonophysics* **152**, 1–17.

Jeffery, G. B. 1922. The motion of ellipsoidal particles immersed in a viscous fluid. *Proc. R. Soc. Lond.* **A (102)**, 161–179.

Jessell, M. W. 1986. Grain boundary migration and fabric development in experimentally deformed octachloropropane. *J. Struct. Geol.* **8**, 527–542.

Lister, G. S. & Snoke, A. W. 1984. *S–C* mylonites. *J. Struct. Geol.* **6**, 617–638.

Masuda, T. & Ando, S. 1988. Viscous flow around a rigid spherical body: a hydrodynamical approach. *Tectonophysics* **148**, 337–346.

Means, W. D. 1983. Microstructure and micromotion in recrystallization flow of octachloropropane: a first look. *Geol. Rdsch.* **72**, 511–528.

Ottino, J. M. 1989. *The Kinematics of Mixing Stretching, Chaos, Transport*. Cambridge University Press, Cambridge.

Passchier, C. W. 1988. The use of Mohr circles to describe non-coaxial progressive deformation. *Tectonophysics* **149**, 323–338.

Passchier, C. W. 1994. Mixing in flow perturbations: a model for the development of mantled porphyroclasts in mylonites. *J. Struct. Geol.* **16**, 733–736.

Passchier, C. W. & Simpson, C. 1986. Porphyroclast systems as kinematic indicators. *J. Struct. Geol.* **8**, 831–844.

Passchier, C. W. & Sokoutis, D. 1993. Experimental modelling of mantled porphyroclasts. *J. Struct. Geol.* **15**, 895–909.

Passchier, C. W., ten Brink, C. E., Bons, P. D. & Sokoutis, D. 1993. δ-objects as a gauge for the stress sensitivity of strain-rate in mylonites. *Earth Planet. Sci. Lett.* **120**, 239–245.

Ramsay, J. G. 1967. *Folding and Fracturing of Rocks*. New York.

Simpson, C. & De Paor, D. G. 1993. Strain and kinematic analysis in general shear zones. *J. Struct. Geol.* **15**, 1–20.

ten Brink, C. E., Bons, P. D. & Passchier, C. W. 1993. Approximate stream functions for flow around rigid objects in shear zones. Abstract supplement No. 2 to *Terra Nova* **5**, 35.

Truesdell, C. 1953. Two measures of vorticity. *J. Rotational Mech. Anal.* **2**, 173–217.

Van Den Driessche, J. & Brun, J.-P. 1987. Rolling structures at large shear strain. *J. Struct. Geol.* **9**, 691–704.

APPENDIX

The way in which deformation parameters are defined is shown in Fig. A1, which is a Mohr representation for a deformation tensor **F** (Passchier 1988):

$$\mathbf{F} = \begin{bmatrix} a & b \\ c & d \end{bmatrix}.$$

Useful equations to determine deformation parameters from the Mohr diagram are:

$$R_f = \frac{1 + e_1}{1 + e_2} = \frac{T + R}{T - R}; \tag{A1}$$

$$W_f = \frac{Q}{R}; \tag{A2}$$

$$A_f = (1 + e_1)(1 + e_2) = (T + R)(T - R); \tag{A3}$$

$$\beta_f = \varphi - \alpha; \tag{A4}$$

where:

$$T = 0.5\sqrt{(a + d)^2 + (b - c)^2} \tag{A5}$$

$$R = 0.5\sqrt{(a - d)^2 + (b + c)^2} \tag{A6}$$

$$Q = 0.5(b - c) \tag{A7}$$

$$S = 0.5(d + a) \tag{A8}$$

$$\sin \alpha = Q/T \tag{A9}$$

$$\sin 2\varphi = \frac{(a - S)S - (c + Q)Q}{RT}. \tag{A10}$$

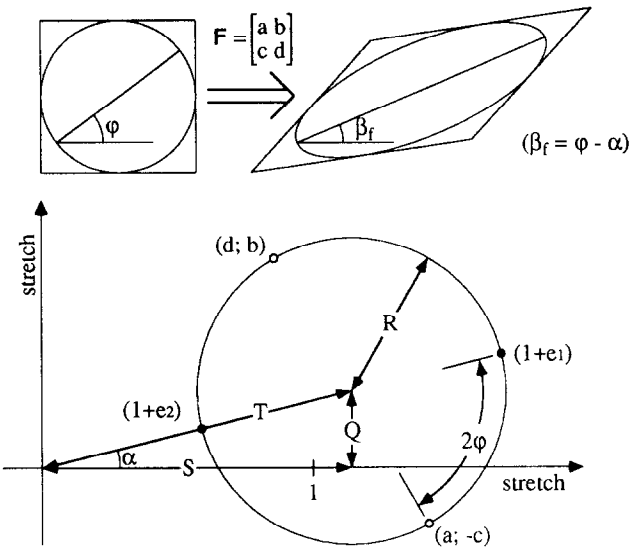

Fig. A1. Top—deformation of a square showing the orientation of the strain ellipse. Bottom—Mohr diagram for the deformation tensor **F**, illustrating the derivation of deformation parameters. See explanation in the text.